



# The Background Interstellar Medium as Observed from Off-order Low-resolution Spitzer-IRS Spectra

C. Boersma , J. D. Bregman , L. J. Allamandola , P. Temi , and A. Maragkoudakis

NASA Ames Research Center, MS 245-6, Moffett Field, CA 94035-1000, USA; [Christiaan.Boersma@nasa.gov](mailto:Christiaan.Boersma@nasa.gov)

Received 2024 July 22; revised 2024 September 10; accepted 2024 September 17; published 2024 November 1

## Abstract

Spitzer “hidden” observations of the background are used to construct a catalog of 4090 spectra and examine the signature of polycyclic aromatic hydrocarbon (PAH) molecules and their connection to extinction by dust. A strong positive correlation is recovered between WISE12,  $E(B - V)$ , and the  $11.2 \mu\text{m}$  PAH band. For  $0.06 \leq E(B - V) \leq 5.0$ , correlations of the  $6.2$ ,  $11.2$ , and  $12.7 \mu\text{m}$  PAH band are positive with  $E(B - V)$ . Three dust temperature regimes are revealed. Correlations with WISE12 are well constrained and that with  $12.7/11.2$  is flat. Decomposition with the NASA Ames PAH IR Spectroscopic Database reveals a tentative positive correlation between the  $6.2/11.2$  and the PAH ionization fraction, while that with  $12.7/11.2$  is slightly negative, suggesting PAH structural changes. The relation with PAH size and  $6.2/11.2$  is negative, while that with  $12.7/11.2$  is positive. Averaging spectra into five  $E(B - V)$  and three  $T_{\text{dust}}$  bins shows an evolution in PAH emission and variations in  $12.7/11.2$ . Database-fits show an increase in  $f_i$  and the PAH ionization parameter  $\gamma$ , but a more stable large PAH fraction. While the largest  $\gamma$ s are associated with the highest  $T_{\text{dust}}$ , there is no one-to-one correlation. The analysis is hampered by low-quality data at short wavelengths. There are indications that PAHs in the more-diffuse backgrounds behave differently from those in the general interstellar medium. However, they are often still associated with larger scale filamentary cloud-like structures. The spectra and auxiliary data have been made available through the Ames Background Interstellar Medium Spectral Catalog and may guide JWST programs.

*Unified Astronomy Thesaurus concepts:* [Interstellar medium \(847\)](#); [Interstellar dust \(836\)](#); [Dust continuum emission \(412\)](#); [Infrared spectroscopy \(2285\)](#); [Astronomy databases \(83\)](#); [Polycyclic aromatic hydrocarbons \(1280\)](#)

## 1. Introduction

The life cycle of interstellar polycyclic aromatic hydrocarbon (PAH) molecules starts with their formation in the ejecta from carbon-rich AGB stars followed by a residency in the interstellar medium (ISM), where they subsequently evolve via processing by ultraviolet (UV) photons. After some  $10^7$  yr, PAHs are incorporated into dark clouds where they are thought to freeze out onto dust grains and are processed further, along with new PAH formation, now via ice grain chemistry. Once new stars form, PAHs are exposed to UV radiation and processed yet again. This PAH-evolution is observed as spectral changes from one environment to another and within individual objects, e.g., in reflection nebulae (RNe) as a function of distance from the illuminating star (see e.g., J. Bregman & P. Temi 2005; C. Boersma et al. 2016). PAHs have been well studied in planetary nebulae (PNe), H II-regions, and RNe, but little work has been done on PAHs in the background, diffuse ISM.

The direct association of dust with PAHs has been inferred from the correlation of IRAS  $100 \mu\text{m}$  measurements with that of the  $3.3 \mu\text{m}$  PAH band strength (M. Tanaka et al. 1996) and with  $4.5$ – $11.7 \mu\text{m}$  spectra (T. Onaka et al. 1996) obtained by the Infrared Telescope in Space (IRTS). While the  $3.3 \mu\text{m}$  data show a correlation with both IRAS  $12 \mu\text{m}$  (PAHs) and the  $100 \mu\text{m}$  (classical dust) data in the intensity range corresponding to the diffuse background ISM, almost all of the mid-IR data sample directions toward dense clouds rather than the

background diffuse ISM. Broadband WISE  $12 \mu\text{m}$  band 3 data was selected to sample PAH emission based on the IRTS results. Consequently, WISE band 3 data is commonly used as a proxy for PAH emission (see e.g., A. M. Meisner & D. P. Finkbeiner 2014; T.-W. Lan et al. 2015).

Utilizing data obtained by the InfraRed Spectrograph (IRS; J. R. Houck et al. 2004) onboard the Spitzer Space Telescope (Spitzer; M. W. Werner et al. 2004) during its cryogenic mission that ended on 2009 May 15, this work generates a catalog of 4090 low-resolution spectra of the background ISM by extracting them from the off-order positions. In turn, this catalog is used to study the PAH emission from the background ISM and its connection to other dust components. The catalog is made available as The Ames Background ISM Spectral Catalog and can be accessed through a comprehensive website.

This paper is organized as follows. Section 2 describes the observations and data reduction, Section 3 sets out the analysis, Section 4 discusses the results, Section 5 draws astronomical implications, Section 6 describes The Ames Background ISM Spectral Catalog, and Section 7 concludes the paper with a summary and its main takeaways.

## 2. Observations

### 2.1. Spitzer

Candidate Spitzer observations were taken from The Nominal Science Operations—Schedule of Executed Science and Calibration Observations, which was obtained from IRSA.<sup>1</sup> The observation log lists 58,575 entries up to the end of the

<sup>1</sup> [irsa.ipac.caltech.edu/data/SPITZER/docs/files/spitzer/spitzer\\_obslog.txt](https://irsa.ipac.caltech.edu/data/SPITZER/docs/files/spitzer/spitzer_obslog.txt)

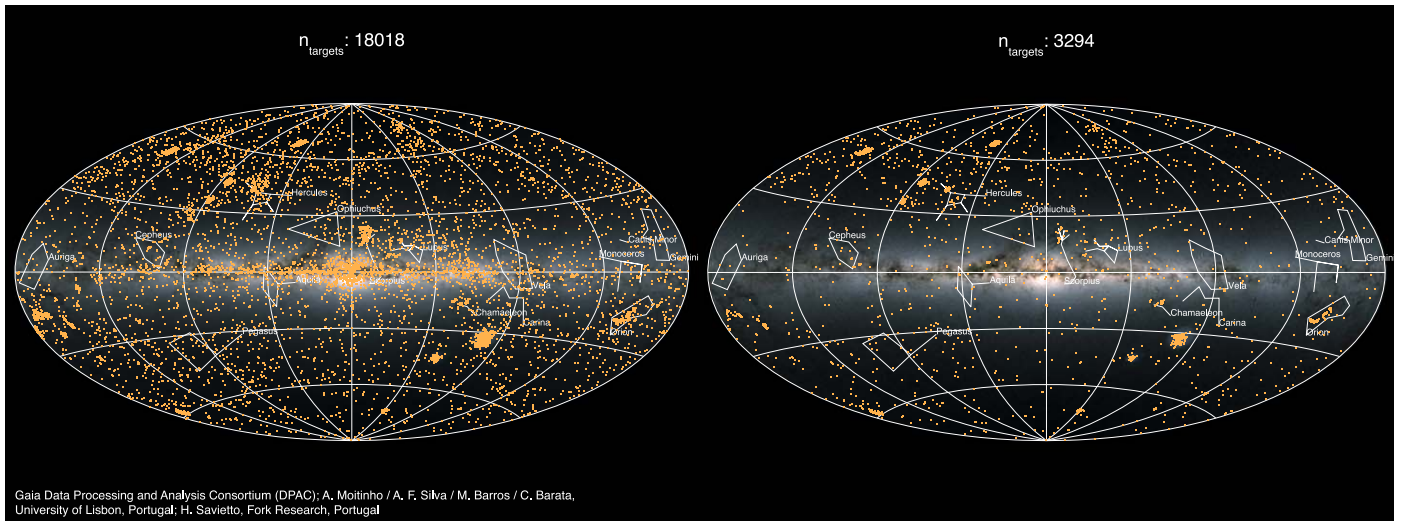


**Figure 1.** Positions of the Spitzer-IRS staring observations considered in this work overlain on a GAIA all-sky color image using an isotropic Aitoff projection. Some well-known constellations are indicated. Left: all 18,018 irsstare observations. Right: the 3294 irsstare observations with 60 or 240 s ramp time and outside  $1^\circ$  of the Galactic plane. See Section 2 for details.

cryogenic mission, of which 18,018 are labeled as  $AOT=irsstare$ . The left panel of Figure 1 shows the positions of these observations on the sky overlain on an all-sky GAIA color image (second data release<sup>2</sup>). To avoid the crowded Milky Way, a  $1^\circ$  exclusion zone around the galactic plane is imposed, i.e., half a degree above and below it, based on the reported target positions in the observation log. This brings the number of IRS staring observations down to 17,600. Next, metadata associated with each observation were retrieved using the API<sup>3</sup> exposed by the Spitzer Heritage Archive (SHA) using the AOR key associated with each observation. Subsequently, these were used to check for short-low (SL) observations and ensure both SL1 ( $7.5 \lesssim \lambda \lesssim 14.5 \mu\text{m}$ ) and SL2 ( $5.2 \lesssim \lambda \lesssim 14.5 \mu\text{m}$ ) orders are present. This brings the number of observations to consider down to 10,190. Lastly, using the same metadata from the SHA the observations were further limited to those having either a ramp time of 60 or 240 s to ensure enough exposure to detect the weak emission associated with the background ISM. This reduced the number of observations to 3294; with 2813 and 481 having 60 and 240 s ramp times, respectively. The galactic positions of these observations are shown in the right panel of Figure 1.

## 2.2. Data Reduction

The raw data associated with each of the 3294 observations were retrieved from the SHA.<sup>4</sup> The CUPID software tool at version 2.0<sup>5</sup> was used to generate basic calibrated data (BCD), taking into account different pointings—traced by the CLNUMPOS FITS header keyword—in a single observation. BCDs were created both with and without using the pipeline’s default dark subtraction. BCDs for a total of 4090 positions were generated, where those having multiple pointings and those only containing peak-up data were taken into account. It is noted that for a few pointings the slit information was missing (PA\_SLIT FITS header keyword). Table A1 in

Appendix A lists the five observations that could not be processed.

Next, spectra were extracted from the BCDs using the The CUbe Builder for IRS Spectra Maps (CUBISM<sup>6</sup>; J. D. T. Smith et al. 2007) tool. CUBISM was modified to allow automation of the process. Spectra were extracted using a  $24 \times 2$  pixel window (see Figure 2 for details) in the off-order position to obtain a background spectrum and saved to disk using the IPAC table format<sup>7</sup> for both the dark- and non-dark-corrected BCDs. The associated headers track relevant information, e.g., remapped center position, target name, program name, pointing, reduction history, etc. The IPAC-formatted tables for the non-dark-corrected spectra have been made publicly available (see Section 6). Figure 3 showcases and compares typical dark and non-dark-extracted spectra. Also shown is an estimate for the zodiacal light spectrum as determined by the Zodiacal Light Model available through IPAC.<sup>8</sup> The figure shows that most of the nondark emission can be attributed to zodiacal light.

Lastly, on- and off-order cross-dispersion profiles are constructed for emission between 11 and  $11.6 \mu\text{m}$ . First, for each target and pointing the Data Collection Event files for a single nod position are combined for the non-dark-subtracted BCDs, FUNCs, and BMASKs. Second, the resulting combined images are collapsed in the cross-dispersion direction after straightening the source trace to achieve a subpixel sampling of the profile. Third, wavelength and order are associated with each data point using available calibration files (`irs_sl_wavesamp-[omask,wave]_v5.fits`). Finally, the cross-dispersion profile between 11 and  $11.6 \mu\text{m}$  is constructed for each exposure and fitted with a Gaussian profile plus an offset. The IDL MPFITPEAK-procedure by Craig Markwardt is used for the fitting, forcing a positive peak and a minimum FWHM of  $2''/355$ , the extent of a point-source. Prior to fitting, the data are sigma clipped over four surrounding elements. Figure 4

<sup>2</sup> [sci.esa.int/gaia/60196-gaia-s-sky-in-color-equirectangular-projection/](https://sci.esa.int/gaia/60196-gaia-s-sky-in-color-equirectangular-projection/)

<sup>3</sup> [sha.ipac.caltech.edu/applications/Spitzer/SHA/help/doc/api.html](https://sha.ipac.caltech.edu/applications/Spitzer/SHA/help/doc/api.html)

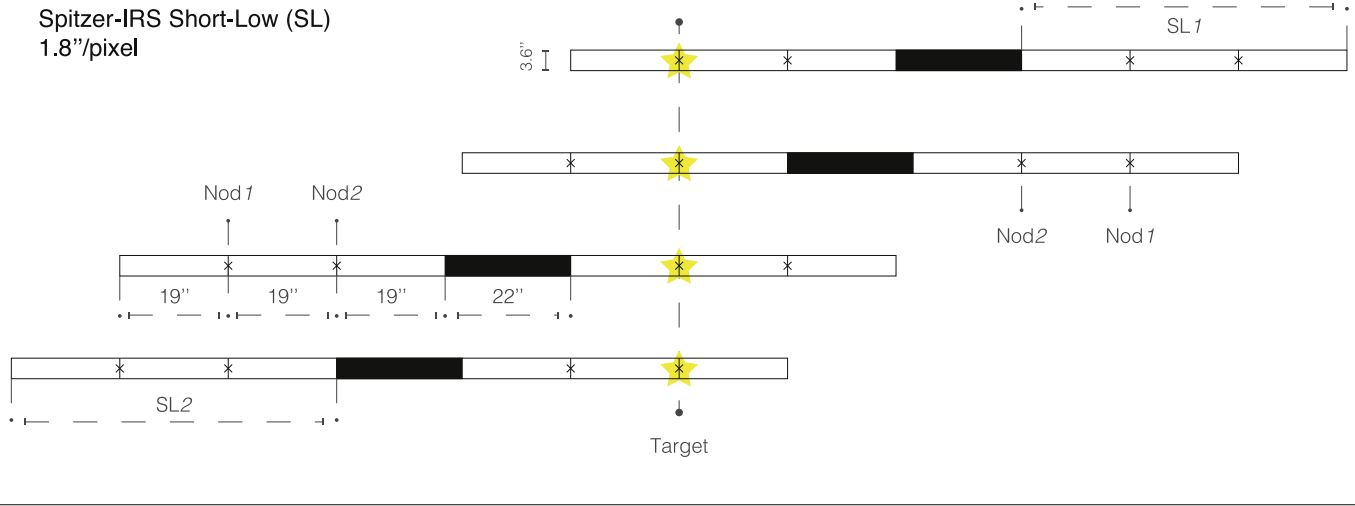
<sup>4</sup> [sha.ipac.caltech.edu/applications/Spitzer/SHA/](https://sha.ipac.caltech.edu/applications/Spitzer/SHA/)

<sup>5</sup> [irsa.ipac.caltech.edu/data/SPITZER/docs/dataanalysisstools/tools/cupid/](https://irsa.ipac.caltech.edu/data/SPITZER/docs/dataanalysisstools/tools/cupid/)

<sup>6</sup> [irsa.ipac.caltech.edu/data/SPITZER/docs/dataanalysisstools/tools/cubism/](https://irsa.ipac.caltech.edu/data/SPITZER/docs/dataanalysisstools/tools/cubism/)

<sup>7</sup> [irsa.ipac.caltech.edu/applications/DDGEN/Doc/ipac\\_tbl.html](https://irsa.ipac.caltech.edu/applications/DDGEN/Doc/ipac_tbl.html)

<sup>8</sup> [irsa.ipac.caltech.edu/data/SPITZER/docs/dataanalysisstools/tools/contributed/general/zodiacallight/](https://irsa.ipac.caltech.edu/data/SPITZER/docs/dataanalysisstools/tools/contributed/general/zodiacallight/)



On-sky geometry when extraction off-order spectra

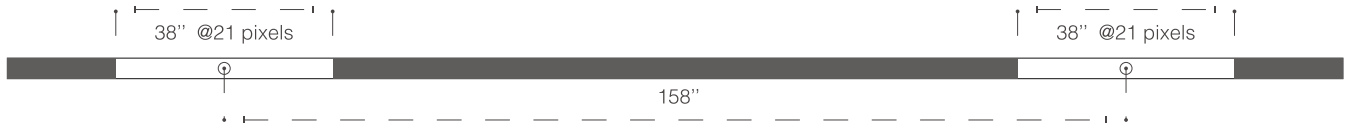


**Figure 2.** Slit layout. The top four narrow rectangles resemble the long slit of the low-resolution (SL) infrared spectrograph (IRS) module onboard Spitzer projected onto the sky. Each slit depicts the position of the target (yellow star) in the slit when employing a nodding strategy. When the target is, in either nod position, on the left half of the slit its light is diffracted by the grating in first order (SL1). Subsequently, when the source is on the right half the light is diffracted in second order (SL2). As a bonus, the SL2 configuration also produces a spectral segment covering  $7.3 \lesssim \lambda \lesssim 8.7 \mu\text{m}$  (SL3). Note that the 22'' part of the slit shaded black is not used. Simultaneously, when the target is observed in one order the background is observed in the other. The on-sky geometry shown at the bottom reveals a spatial separation of 158'' between the SL1 and SL2 observations of the background and a  $3.6'' \times 38''$  ( $2 \times 21$  pixels) overlapping aperture. NB the observations considered in this work all make use of the depicted nodding strategy.

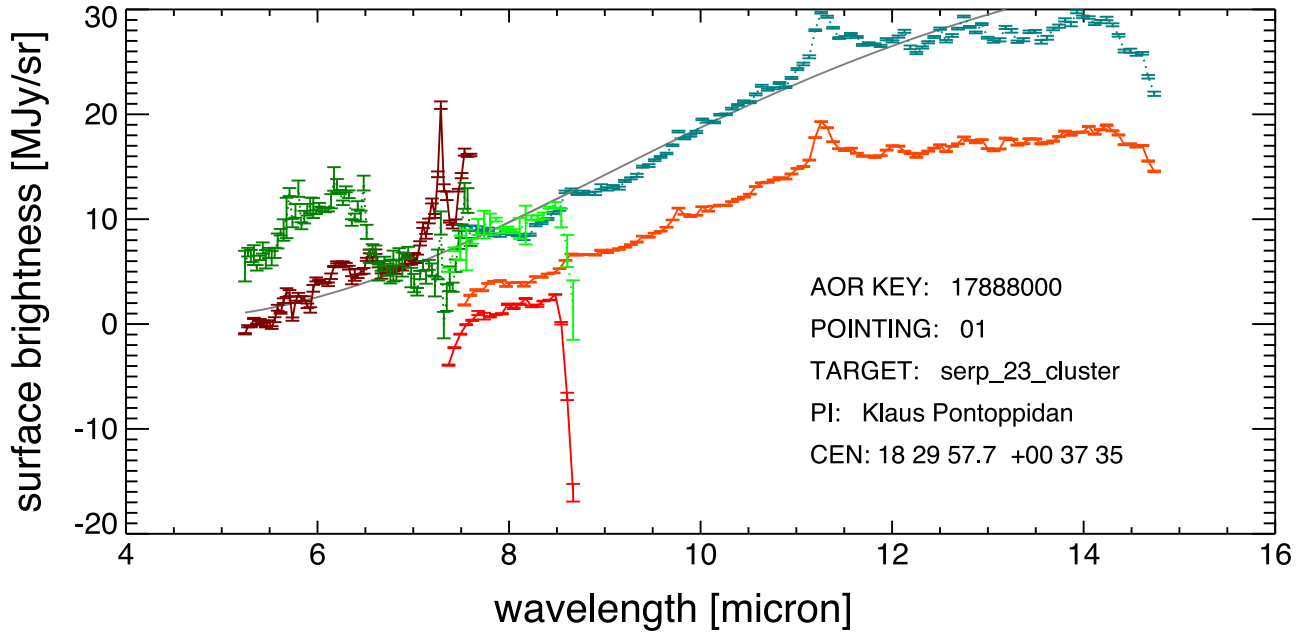


**Figure 3.** Extracted spectra. The SL1, 2, and 3 orders for the dark corrected spectrum have been colored light red, red, and dark red, respectively. Those for the nondark corrected spectrum light green, green, and dark green, respectively. The modeled zodiacal light is shown as the gray line. See Section 2.2 for details.

provides an example of the extracted and fitted cross-dispersion profile for the same target and pointing as shown in Figure 3 after shifting its center to 0'' and subtracting the offset. The figure reveals slightly extended PAH emission originating from the target with a FWHM of about  $2.5''$ , while the signal from the background is spatially unresolved, thus fully extended. It

is noted that for all background cross-dispersion profiles the PAH signal is spatially unresolved.

### 3. Analysis

To isolate any PAH emission bands in the background spectra, a broad continuum is subtracted. This continuum

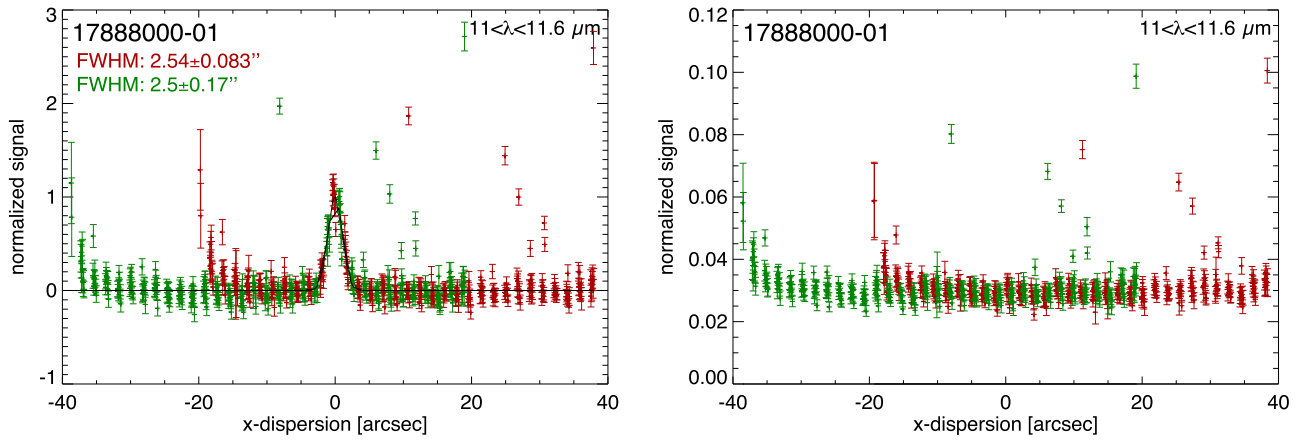


**Figure 4.** Determined and fitted cross-dispersion profiles for the  $11.2\ \mu\text{m}$  PAH band. The two colors represent the two different nod positions. Left: science target. Right: background.

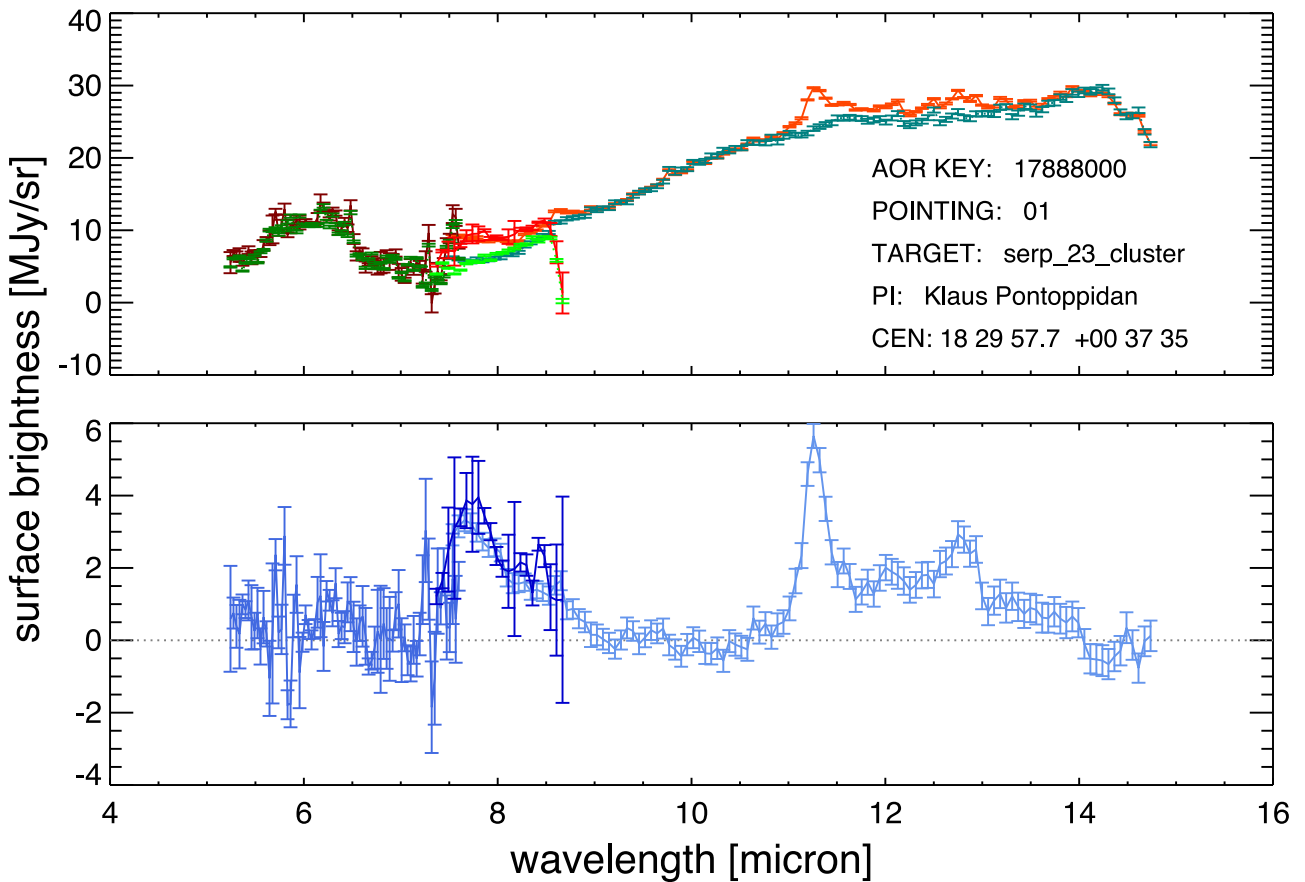


**Figure 5.** Top: Constructed broadband continuum (greens) matched to the non-dark-corrected spectrum (reds) from Figure 6. Bottom: resulting background spectrum from subtracting the broadband continuum from the non-dark-corrected spectrum. See Section 3 for details.

primarily consists of low surface brightness zodiacal light (see Figure 3), but at SL2 wavelengths is dominated by the IRS' detector response and appears as a broad discrete feature centered around  $6\ \mu\text{m}$ . Removing this continuum is achieved in three steps. First an average zodiacal light spectrum is constructed from the non-dark-subtracted spectra that fall below  $b = -60^\circ$  using a weighted mean. The resulting zodiacal light spectrum is the average of 108 and 15 spectra with 60- and 240 s ramp times, respectively. Second, this spectrum is scaled and added to a 1st-order polynomial to match the emission at parts of the SL1 spectrum not affected by PAH

emission. For the SL2 spectrum the average zodiacal spectrum is only scaled. Wavelength elements between 9 and 11 and beyond  $13.5\ \mu\text{m}$  are used to set the continuum level for SL1, while for SL2 wavelength elements between  $5.7$  and  $5.87\ \mu\text{m}$  are selected. Third, the continuum constructed this way is subtracted. Figure 5 demonstrates this approach for the spectrum in Figure 3. Next, the resulting difference spectrum, e.g., that shown in the bottom panel of Figure 5, is integrated over intervals associated with known PAH emission. For the  $12.7$ ,  $11.2$ , and  $6.2\ \mu\text{m}$  PAH bands integration ranges are set as  $12.2$ – $13.1$ ,  $10.5$ – $11.7$ , and  $5.9$ – $6.4\ \mu\text{m}$ , respectively. Because

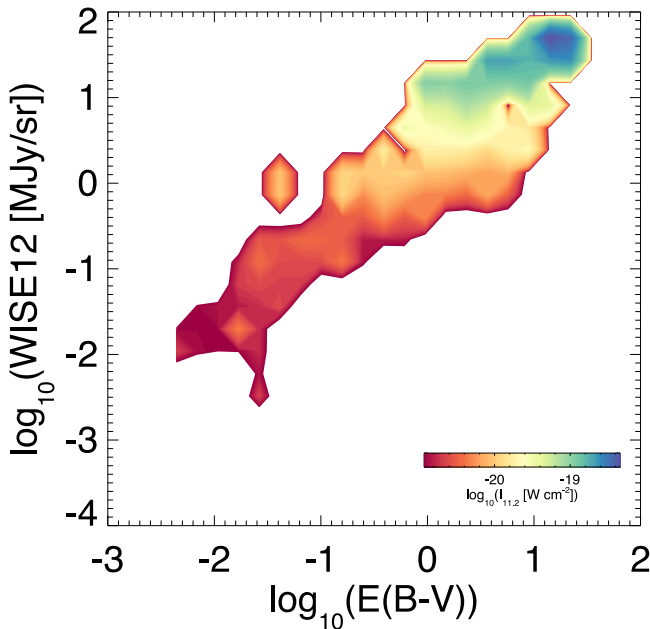


**Figure 6.** WISE12 band vs.  $E(B - V)$  for target positions with a WISE12 band of at least  $1 \times 10^{-4}$  MJy sr $^{-1}$  and an associated uncertainty in the 11.2  $\mu$ m PAH band strength of less than  $3 \times 10^{-21}$  W cm $^{-2}$ . The 11.2  $\mu$ m PAH band strengths are shown using (filled) contours (logarithmically scaled).

the 7.7  $\mu$ m PAH emission complex is split across SL1 and SL2 it is not considered here.

## 4. Discussion

### 4.1. PAHs and Dust Extinction

The determined PAH band strengths are compared to extinction measurements, where the latter are retrieved from the Galactic Dust Reddening and Extinction service at IPAC<sup>9</sup> (IRSA 2022). The returned information has a spatial resolution of five arcminutes and includes  $E(B - V)$ , 100  $\mu$ m emission, and the dust temperature. Here, the values at the reference pixel (RefPixel) are used. As an alternative measure, the WISE 12  $\mu$ m full-sky dust map<sup>10</sup> is also considered. The 430, 8000  $\times$  8000 pixel “cleaned” tiles covering the entire sky at a spatial resolution of 6 $''$ .5 were obtained and the WISE12  $\mu$ m flux and standard error were computed over a 3 pixel circular aperture.

Figure 6 shows the strength of the WISE12 band versus  $E(B - V)$  for background positions with a WISE12 band of at least  $1 \times 10^{-4}$  MJy sr $^{-1}$  and an associated uncertainty in the 11.2  $\mu$ m PAH band strength of less than  $3 \times 10^{-21}$  W cm $^{-2}$ . The 11.2  $\mu$ m PAH band strengths are shown as the (filled) contours. The contours have been constructed from a 21  $\times$  21 pixel image of the average 11.2  $\mu$ m PAH band strength of the points falling in a single pixel. The figure establishes the known correlation between WISE12 and  $E(B - V)$  and shows that the 11.2  $\mu$ m PAH band strength correlates as well.

Figure 7 presents six correlation plots that involve either WISE12 or  $E(B - V)$  and the PAH band strengths for data with a signal-to-noise ratio (SNR) of at least 3 and  $0.06 \leq E(B - V) \leq 5.0$ . In each panel the data points have been color

coded according their associated dust temperature. Trend lines determined by fitting a first-order polynomial, not taking into account uncertainties, have been overlain. For each correlation the linear correlation coefficient  $R^2$ , taking uncertainties into account, has been provided.

The figure shows that the 6.2  $\mu$ m PAH band is significantly hampered by poor SNR as can be inferred from Figure 5 and the top-left and middle-right panels of Figure 7, where only 83 data points have a SNR  $\geq 3$ . In contrast, the correlations involving the other two PAH band intensities count almost ten times as many points. The correlations of the 11.2 and 12.7  $\mu$ m PAH band intensities with the WISE12 band are far more significant with a  $R^2$  of 0.79 and 0.84, respectively. In addition, the correlations are quite tight and show, overall, an increase in dust temperature with an increase in both the PAH band intensity and WISE12 band.

Turning to the correlations of the PAH band intensities with  $E(B - V)$ , while the trend lines hint at tentative correlations, none are supported by their  $R^2$  values. Though, there appears to be a stratification with an increase in PAH band strengths with dust temperature. That is, lower temperatures are associated with lower PAH band strength intensities. This is further explored in Figure 8, which plots the correlations with  $E(B - V)$  using a linear scale.

When plotting the PAH band strength correlations with  $E(B - V)$  on a linear scale (Figure 8), stratification with dust temperature becomes quite apparent and hints at three discrete temperature regimes. To emphasize this, trend lines have been added by separately fitting the data for  $T_{\text{dust}} < 18$ ,  $18 \leq T_{\text{dust}} \leq 20$ , and  $T_{\text{dust}} > 20$  K. For all three PAH band strengths, points falling in the lowest temperature bin have the weakest correlation per  $R^2$  and, except for 6.2  $\mu$ m, those falling in the highest bin have the strongest. The only meaningful correlation with the 6.2  $\mu$ m PAH band strength is for  $18 \leq T_{\text{dust}} \leq 20$ . Overall, the trend line for temperatures  $> 20$  K visually matches best the correlation of the 11.2  $\mu$ m PAH band strength with  $E(B - V)$ , which is reflected by having the best  $R^2$  (0.84).

A likely explanation for the observed bifurcation is that those background positions with a higher dust temperature, and subsequently stronger PAH band emission, are influenced by an additional radiation source rather than the interstellar radiation field alone. This could either be because they are still receiving some portion of the radiation from the on-target source or the off-target background position happens to fall near a not too distant radiation source in, for example, a crowded star-forming region like the Orion Molecular Cloud.

Figure 9 presents the 12.7/11.2  $\mu$ m PAH band strength ratio versus  $E(B - V)$ . Since both bands are obtained from the same spectral segment (SL1), their ratios are relatively well constrained. Traditionally the 12.7/11.2  $\mu$ m PAH band strength ratio has been considered a measure for PAH edge structure, notably the ratio of (duo+trio)/solo hydrogens. However, the ratio typically also shows a strong correlation with the 6.2/11.2  $\mu$ m PAH band strength ratio, which is considered a tracer for PAH charge (e.g., S. Hony et al. 2001; C. Boersma et al. 2014b). The figure reveals a ratio hovering around 0.7 for all the backgrounds, with  $R^2$  indicating no correlation, and no obvious stratification with dust temperature is discerned. This lack of stratification of the 12.7  $\mu$ m band is more fully explored in the next section.

<sup>9</sup> [irsa.ipac.caltech.edu/applications/DUST/docs/dustProgramInterface.html](https://irsa.ipac.caltech.edu/applications/DUST/docs/dustProgramInterface.html)

<sup>10</sup> [faun.rc.fas.harvard.edu/ameisner/wssa/](https://faun.rc.fas.harvard.edu/ameisner/wssa/)

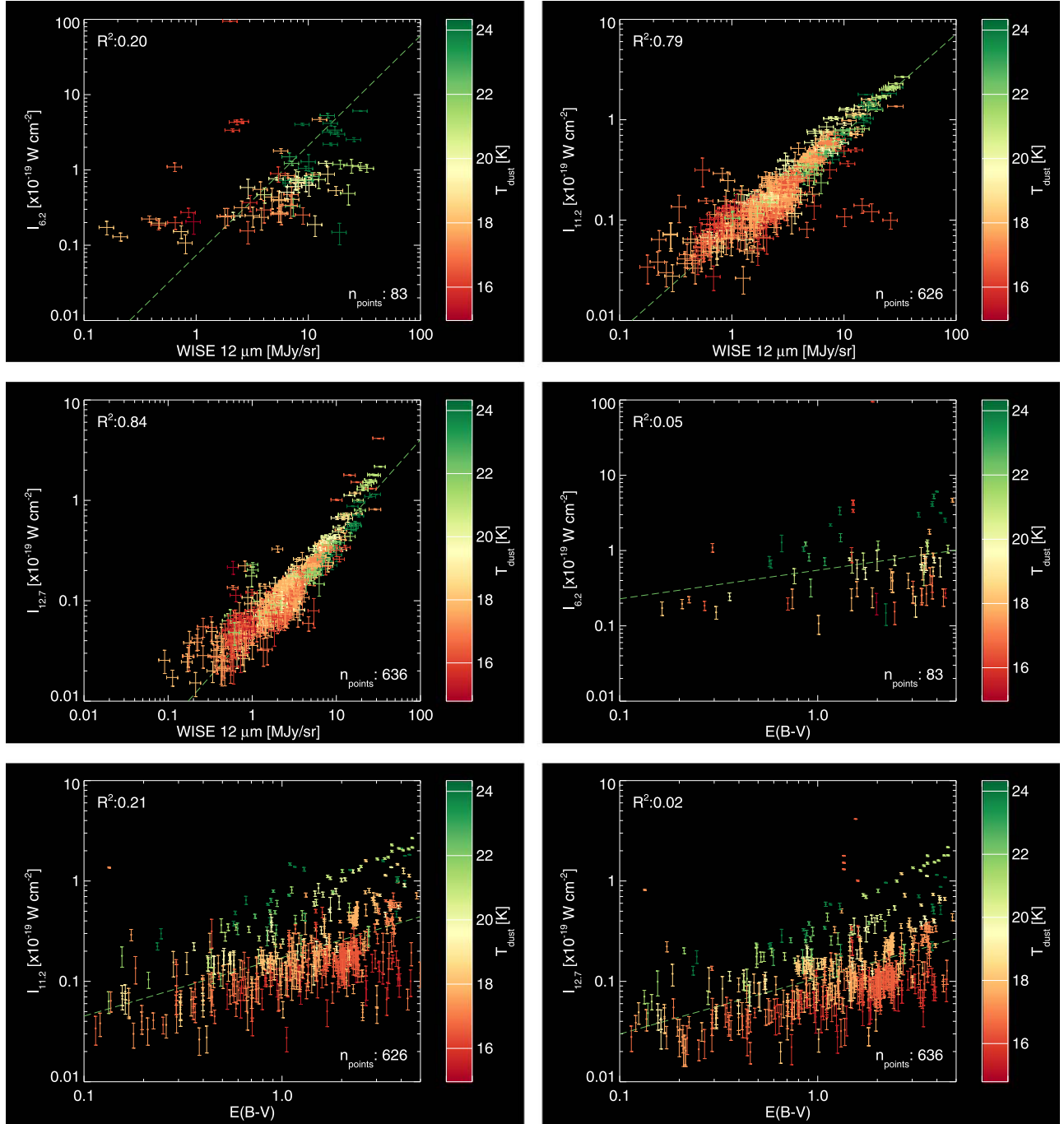


**Figure 7.** Correlation plots involving either WISE12 or  $E(B - V)$  and the 6.2, 11.2 and 12.7  $\mu\text{m}$  PAH band strengths. Each data point is color coded according to its associated dust temperature. The data have a  $\text{SNR} \geq 3$  and  $0.06 \leq E(B - V) \leq 5.0$ . Trend lines determined by fitting the data have been overlain. For each correlation the linear correlation coefficient  $R^2$ , taking uncertainties into account, has been provided. See Section 4.1 for details.

#### 4.2. Emission Lines

For many astronomical objects, the 12.7  $\mu\text{m}$  PAH emission band blends with the 12.8  $\mu\text{m}$  Ne II and the 12.3  $\mu\text{m}$  H<sub>2</sub> S(2) lines. These contributions to the 12.7  $\mu\text{m}$  PAH band are removed using the approach from M. J. Shannon et al. (2015). Here, an emission-line-free 12.7  $\mu\text{m}$  PAH band is used as a template to fit the feature. The template used is that from C. Boersma et al. (2018), which is extracted from Spitzer-IRS observations of the RN NGC 7023. The fitting region is selected such that it excludes resolution elements affected by the two emission lines. Figure 10 demonstrates the approach

for the spectrum shown in Figures 3 and 5. The figure shows that some of the 12.7  $\mu\text{m}$  emission can be attributed to Ne II, while any contribution from the H<sub>2</sub> S(2) line could not be reliably identified (i.e.,  $I_{\text{H}_2} < 0 \text{ W cm}^{-2}$ ).

Figure 11 reproduces the correlations presented in Figure 7 that involve the 12.7  $\mu\text{m}$  PAH band, but now uses the strength determined from the approach described above (PAH<sub>12.7</sub>). The figure shows that there is a drastic decrease in the number of points that pass the SNR threshold (3), with that of the PAH<sub>12.7</sub> versus WISE12 and  $E(B - V)$  going from 399 to 212 and 636 to 244, respectively. This would suggest that for many, if not

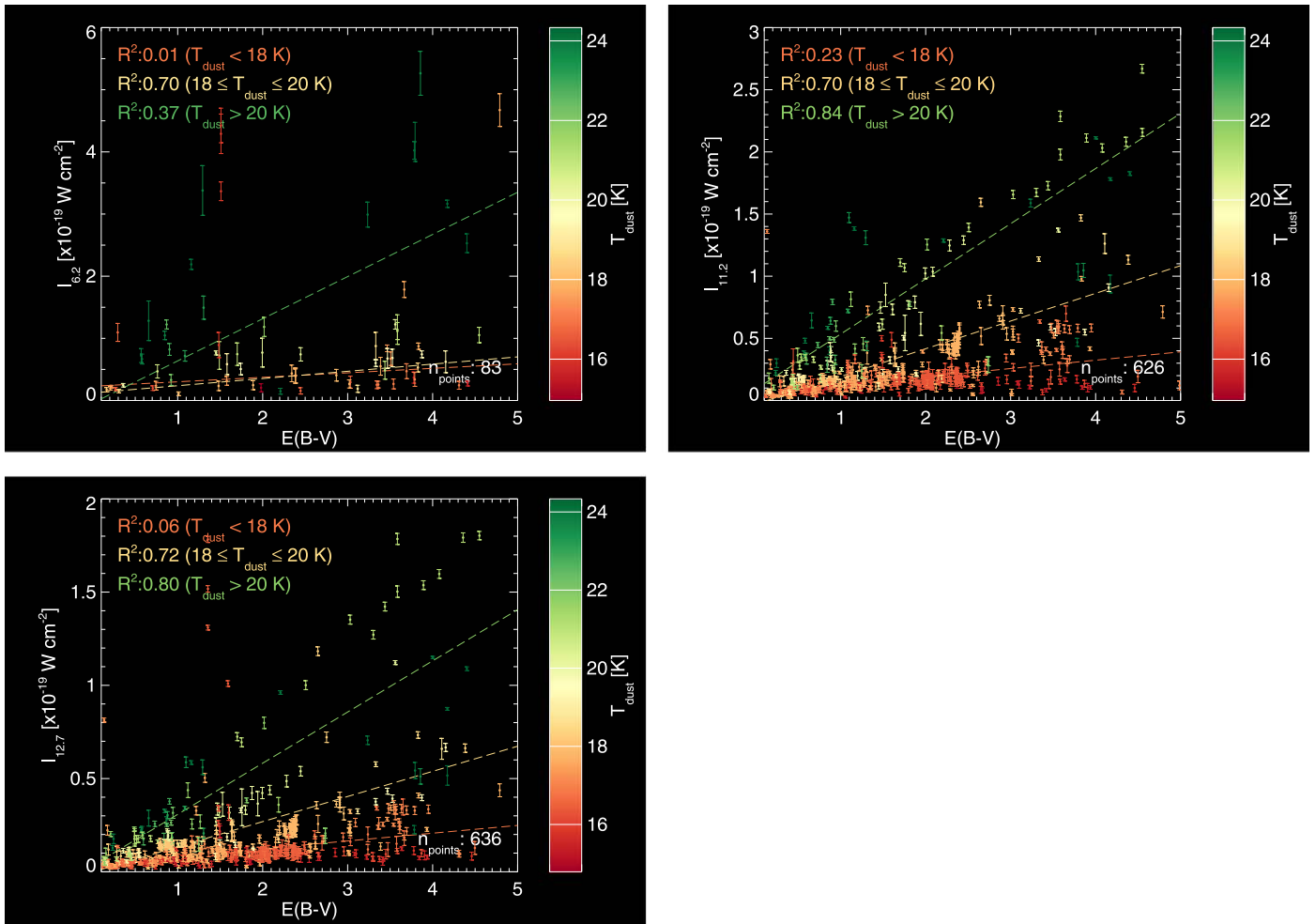


**Figure 8.** Correlation of the 6.2 (top-left), 11.2 (top-right), and 12.7  $\mu\text{m}$  (bottom-left) PAH band strength with  $E(B - V)$  presented on a linear scale counter to the logarithmic scale used in Figure 7. Each data point is color coded according to its dust temperature. The data have a  $\text{SNR} \geq 3$  and  $0.06 \leq E(B - V) \leq 5.0$ . Trend lines determined by fitting the data, taking uncertainties into account, for three separate dust temperature intervals have been overlain. For each temperature interval the linear correlation coefficient  $R^2$ , that takes uncertainties into account, has been provided. See Section 4.1 for details.

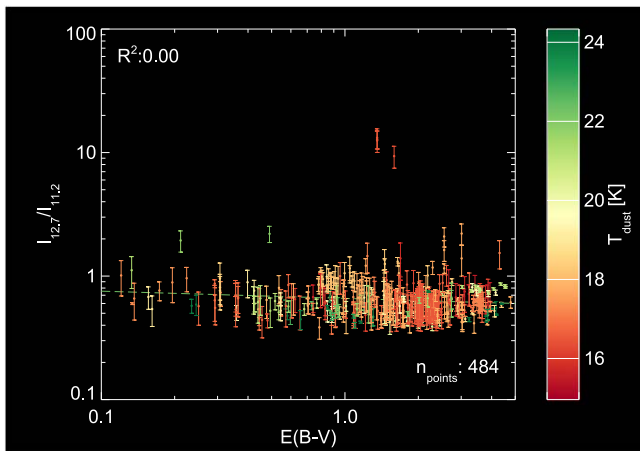


**Figure 9.** The 12.7/11.2  $\mu\text{m}$  PAH band strength ratio vs.  $E(B - V)$ . Each data point is color coded according to its associated dust temperature. The data have a  $\text{SNR} \geq 3$  and  $0.06 \leq E(B - V) \leq 5.0$ . A trend line determined by fitting the data has been overlain. Provided is, taking uncertainties into account, the linear correlation coefficient  $R^2$ . See Section 4.1 for details.

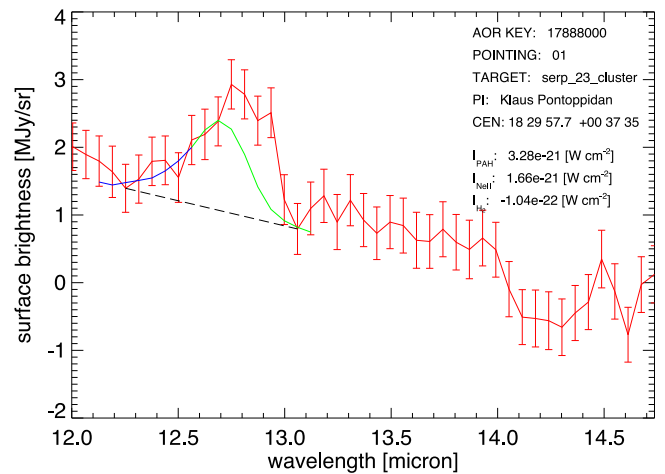


**Figure 10.** Disentangling Ne II, H<sub>2</sub>, and 12.7  $\mu\text{m}$  PAH band emission by establishing a straight-line continuum (gray-dashed line) and fitting a scaled generic 12.7  $\mu\text{m}$  PAH profile (blue- and green-solid line) from the RN NGC 7023. The fitted profile is shown, where any excess between the observations (red) and the blue and green is attributed to H<sub>2</sub> S(2) and Ne II emission, respectively. See Section 4.2 for details.

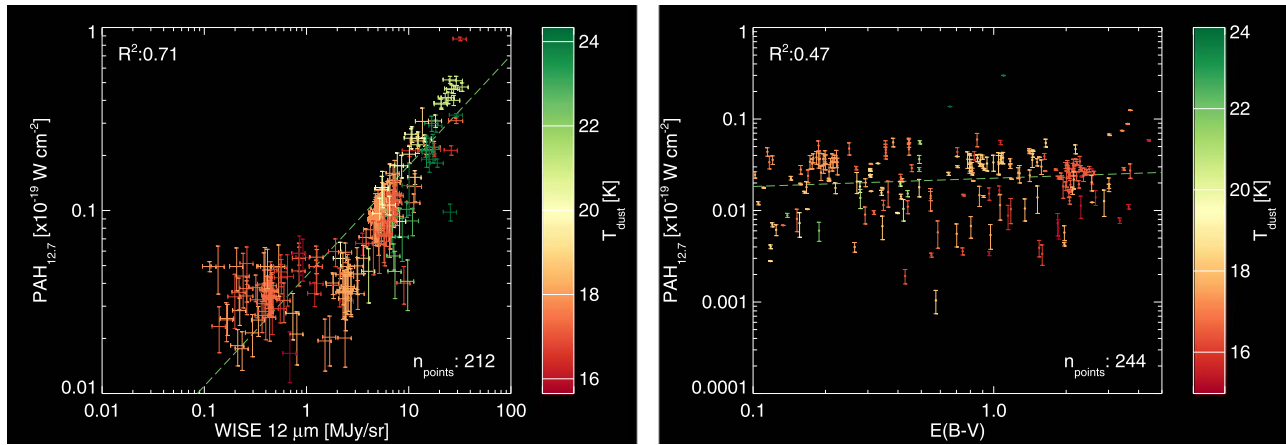


**Figure 11.** The correlations from Figure 7 involving the 12.7  $\mu\text{m}$  PAH band strength presented now using  $\text{PAH}_{12.7}$  instead of  $I_{12.7}$ . Trend lines determined by fitting the data have been overlain. For each correlation the linear-correlation coefficient  $R^2$ , which takes uncertainties into account, has been provided. See Section 4.2 for details.

most, background observations the emission at 12.7  $\mu\text{m}$  is affected strongly by line emission.

In terms of WISE12, above a surface brightness of  $\sim 3 \text{ MJy sr}^{-1}$  the correlation with  $\text{PAH}_{12.7}$  seen in Figure 7 is maintained. However, below this value  $\text{PAH}_{12.7}$  flattens out around  $0.05 \times 10^{-19} \text{ W cm}^{-2}$ , albeit with a significant intrinsic spread. Though, overall the correlation remains strong with  $R^2$  dropping only from 0.84 to 0.71. A rather unlikely explanation for the flattening out would be that the correlation seen in Figure 7 is initially driven solely by line emission and that any background  $\text{PAH}_{12.7}$  emission is absent—Ne II emission is typically associated with distinct astronomical objects like H II regions and RNe. A far more plausible explanation is that the already low SNR for these low-intensity points is not enough to confidently identify and remove any line emission. On top of that, the 12.7  $\mu\text{m}$  PAH band is not universal and the emission template taken from NGC 7023 likely not characteristic for *all* background spectra.

Regarding  $E(B-V)$ , the visually spurious correlation with  $I_{12.7}$  present in Figure 7 is now entirely absent, flattened out, and hovering around  $0.02 \times 10^{-19} \text{ W cm}^{-2}$  in the  $\text{PAH}_{12.7}$  case. Though, there is two orders ( $\sim 0.001$ – $0.1$ ) of intrinsic scatter,  $R^2$  seemingly improves from 0.02 to 0.47, and the obvious stratification with dust temperature is now gone.

Figure 12 correlates  $E(B-V)$  with the  $\text{PAH}_{12.7}/11.2 \mu\text{m}$  PAH band strength as a counterpart to Figure 9 that uses  $I_{12.7}$  instead. Again, the number of viable data points drops significantly, going from 484 down to 160. The visually apparent decrease in the ratio with  $E(B-V)$  is perhaps somewhat more prominent here, with the flattening out occurring around  $E(B-V) \simeq 1.0$  and hovering at a  $\text{PAH}_{12.7}/11.2 \mu\text{m}$  ratio of 0.2, down from  $\sim 0.7$  in Figure 9. Here, again  $R^2$  seems to suggest a somewhat stronger correlation, albeit still marginal.

#### 4.3. Spectroscopic Database Fitting

Turning to the library of computed spectra at version 3.20 of the NASA Ames PAH IR Spectroscopic Database (hereafter PAHdb;<sup>11</sup> C. W. Bauschlicher et al. 2010; C. Boersma et al. 2014a; C. W. Bauschlicher et al. 2018; A. L. Mattioda et al. 2020), PAH emission spectra are synthesized for an excitation energy of 7 eV and used to perform a fit to each background

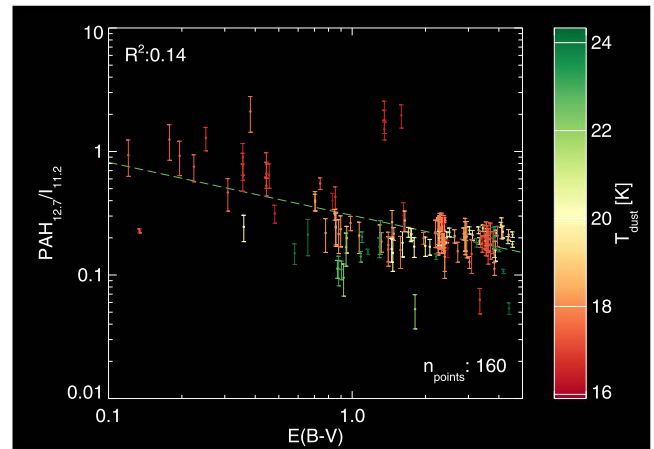


**Figure 12.**  $\text{PAH}_{12.7}/11.2 \mu\text{m}$  PAH band strength ratio. Each data point is color coded according to its associated dust temperature. The data have a  $\text{SNR} \geq 3$  and  $0.06 \leq E(B-V) \leq 5.0$ . A trend line determined by fitting the data has been overlain. Provided is, taking uncertainties into account, the linear correlation coefficient  $R^2$ . See Section 4.2 for details.

spectrum using software tools also provided by PAHdb. The propagated observational uncertainties are taken into account and, to obtain errors for the derived ionization- ( $f_i \equiv n_{\text{cation}} / (n_{\text{cation}} + n_{\text{neutral}})$ ) and large-PAH fraction ( $f_{\text{large}}; N_{\text{carbon}} > 50$ ), a Monte Carlo technique is employed in which the spectra are permuted uniformly within the observational uncertainties and refitted 1024 times. The error ( $\sigma_{\text{SL1}}$ ) is computed as the area of the absolute value of the residual over the area of the astronomical spectra. The integration is done in frequency-space ( $\text{cm}^{-1}$ ) as it is linear in energy. See C. Boersma et al. (2018) for a description of the employed modeling and a discussion of potential caveats. The mean and standard deviation of  $f_i$  and  $f_{\text{large}}$  are subsequently determined for each spectrum. Figure 13 presents the results following this approach for the spectrum shown in Figure 5 and indicates both the single-run and Monte Carlo derived values for  $\sigma_{\text{SL1}}$ ,  $f_i$ , and  $f_{\text{large}}$ . Note that any potential emission lines were not removed (see Section 4.2). The figure shows a reasonably good fit in the SL1 region with  $\sigma_{\text{SL1}}$  of 0.17 for the nonperturbed case, which matches general expectations (e.g., A. Maragkou-dakis et al. 2022). The permuted average error is larger at  $0.23 \pm 0.08$  and reflects the considerable uncertainty on the

<sup>11</sup> [www.astrochemistry.org/pahdb/](http://www.astrochemistry.org/pahdb/)

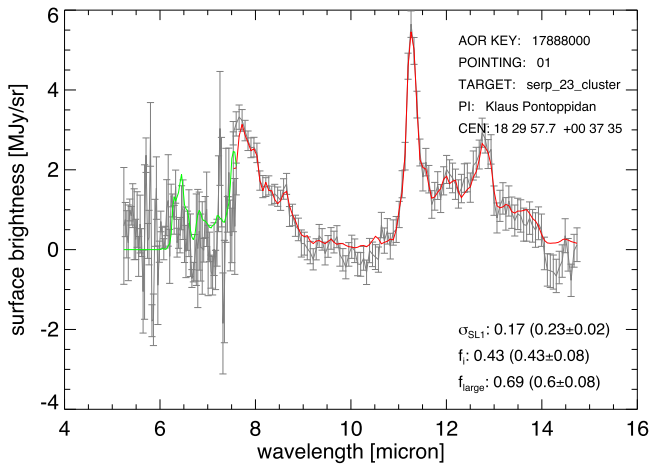


**Figure 13.** PAHdb-fit (SL1 = red, SL2 = green) to the background spectrum (in gray) from Figure 5. Indicated are the single-run error ( $\sigma_{\text{SL1}}$ ), cation- ( $f_i$ ) and large-PAH ( $f_{\text{large}}$ ) fractions and, in parenthesis, the corresponding values with their associated uncertainties from a Monte Carlo technique. See Section 4.3 for details.

data. However,  $f_i$  and  $f_{\text{large}}$  are more consistent at 0.43 and  $0.43 \pm 0.08$  and  $0.69$  and  $0.60 \pm 0.08$ , respectively. Assessment of the fit to the SL2 segment of the spectrum is significantly hampered for this particular background spectrum due to its poor quality, which is unfortunately also the case for most of the other background spectra.

The top two panels in Figure 14 present the 6.2/11.2 (left panel) and 12.7/11.2  $\mu\text{m}$  (right panel) PAH band strength ratios plotted against the Monte Carlo derived  $f_i$ , while the two middle panels do the same for  $f_{\text{large}}$ . The two bottom panels of Figure 14 take the PAH<sub>12.7</sub> PAH band strength instead of  $I_{12.7}$ . Trend lines have been added, constructed from straight-line fits to the data, and  $R^2$  values that take uncertainties into account have been provided. Because of the 6.2  $\mu\text{m}$  PAH band falling in the poor-quality SL2 part of the spectrum, the number of points in the correlations involving it are sparse (64).

Notwithstanding the low number of 6.2/11.2  $\mu\text{m}$  data points, an interesting trend emerges from Figure 14 for the correlations involving the 12.7  $\mu\text{m}$  PAH band (as reflected by their  $R^2$  values). While none of the correlations are particularly strong, the 6.2/11.2  $\mu\text{m}$  PAH band strength versus ionization fraction,  $f_i$ , shows an overall positive trend while that of the 12.7/11.2  $\mu\text{m}$  PAH band strength versus  $f_i$  hints at a negative trend. This is somewhat surprising as a positive correlation between the 6.2/11.2 versus 12.7/11.2  $\mu\text{m}$  PAH band strength ratio has been well established for ISM sources (e.g., S. Hony et al. 2001; C. Boersma et al. 2014b). As shown in the lower two frames of the figure, this tentative negative trend also holds when considering PAH<sub>12.7</sub> instead of  $I_{12.7}$ , where  $R^2$  improves somewhat. Turning to the large PAH fraction,  $f_{\text{large}}$ , the negative trend with the 6.2/11.2  $\mu\text{m}$  PAH band strength ratio is again surprising as the correlation between  $f_i$  and  $f_{\text{large}}$  is generally shown to be positive for ISM sources (e.g., C. Boersma et al. 2015). The same holds for the 12.7/11.2  $\mu\text{m}$  PAH band strength ratio. This unexpected behavior strongly suggests that PAH edge structure is an important *variable* parameter that should be considered when analyzing (diffuse) ISM PAH background spectra, particularly when using ratios of individual band strengths as proxies for single PAH properties such as charge and size. As done here, individual bands are often normalized to the strong, well-defined 11.2  $\mu\text{m}$  band. However,

the 11.2, 12.2, 12.7, 13.5, and 14.2  $\mu\text{m}$  PAH bands are produced by CH out-of-plane bending motions ( $\text{CH}_{\text{oop}}$ ), associated with solo, duo, trio, quartet, and quintet adjacent hydrogen atoms per edge ring, respectively (e.g., S. Hony et al. 2001). The number of these different hydrogen adjacency types depend on PAH structure and size, with small and irregularly shaped PAHs generally carrying substantially more duo through quintet hydrogens than solo hydrogens, while very large, compact structures with straight edges are dominated by solo hydrogens. The relative intensities of these bands vary with PAH size and structure. Thus, one could argue here that, when considering the 12.7/11.2  $\mu\text{m}$  PAH band strength ratio as a pure measure for PAH edge structure, as PAH size increases the relative number of solo hydrogens increases and the 11.2  $\mu\text{m}$  increases, causing the 12.7/11.2  $\mu\text{m}$  PAH band strength ratio to decrease.

Of course, the  $R^2$  values are not particularly convincing, though some of that could be driven by the outliers. In addition, the results are likely susceptible to the systematic effect of the poor quality of much of the SL2 data. Nonetheless, as illustrated by Figure 13, the fit to the 6.2  $\mu\text{m}$  band is somewhat constrained by the error bars. This points to the importance of having a complete  $\sim 5\text{--}15 \mu\text{m}$  spectrum when fitting (see e.g., C. Boersma et al. 2015).

#### 4.4. PAH Spectra Averaged by $E(B - V)$ and $T_{\text{dust}}$

To increase spectral fidelity, Figure 15 takes the background SL1 and SL2 spectra (in gray) that have an uncertainty associated with the 11.2  $\mu\text{m}$  PAH band strength of less than  $3 \times 10^{-21} \text{ W cm}^{-2}$  and averages their broadband continuum subtracted spectra, normalized to the emission at 10  $\mu\text{m}$ , across five  $E(B - V)$  and three  $T_{\text{dust}}$  bins. The figure shows a steady increase in the overall PAH emission when moving both toward higher  $E(B - V)$  values and dust temperatures. This is accompanied by changes in the relative strengths of the 11.2 and 12.7  $\mu\text{m}$  PAH bands. Especially noticeable is the increased fidelity of the SL2 segment when moving toward higher  $E(B - V)$  and  $T_{\text{dust}}$  values.

The average PAH spectra are, as in Section 4.3, fitted using PAHdb, and show generally good matches in the SL1 region of the spectra. However, the poor SNR at the shorter wavelengths covered by the SL2 segment are poorly constrained for all but the bins with the higher  $E(B - V)$  and  $T_{\text{dust}}$  values. Note that the SL3 bonus order has been discarded. The figure indicates both the single-run total error ( $\sigma$ ) and that for the SL1 segment alone  $\sigma_{\text{SL1}}$ , as well as  $f_i$  and  $f_{\text{large}}$  with their associated uncertainties derived from the fit using a Monte Carlo technique.  $\sigma$  and  $\sigma_{\text{SL1}}$  systematically drop as  $E(B - V)$  increases.  $f_i$  generally increases when moving up an  $E(B - V)$  bin or crossing a  $T_{\text{dust}}$  boundary. Compared to  $f_i$ ,  $f_{\text{large}}$  shows less variance, typically staying between 0.4 and 0.5.

The almost systematic variations observed in  $f_i$ , and perhaps  $f_{\text{large}}$  less so, imply altered PAH populations driven by changing astrophysical environments. This can be quantified by turning to the PAH ionization parameter  $\gamma$ , which relates the ionization state of the PAH population to the strength of the radiation field ( $G_0$ ), the electron density ( $n_e$ ), and the temperature of the gas ( $T_{\text{gas}}$ ) as  $\gamma \propto G_0 T_{\text{gas}}^{1/2} / n_e$  (see A. G. G. M. Tielens 2005). Figure 15 provides the PAH ionization parameter  $\gamma$  inferred from the fit as  $2.66 \cdot f_i / f_0 [\times 10^4 \text{ K}^{1/2} \text{ cm}^4]$ , where  $f_0$  is the neutral PAH fraction (e.g., C. Boersma et al. 2018). These are listed in Table 1.

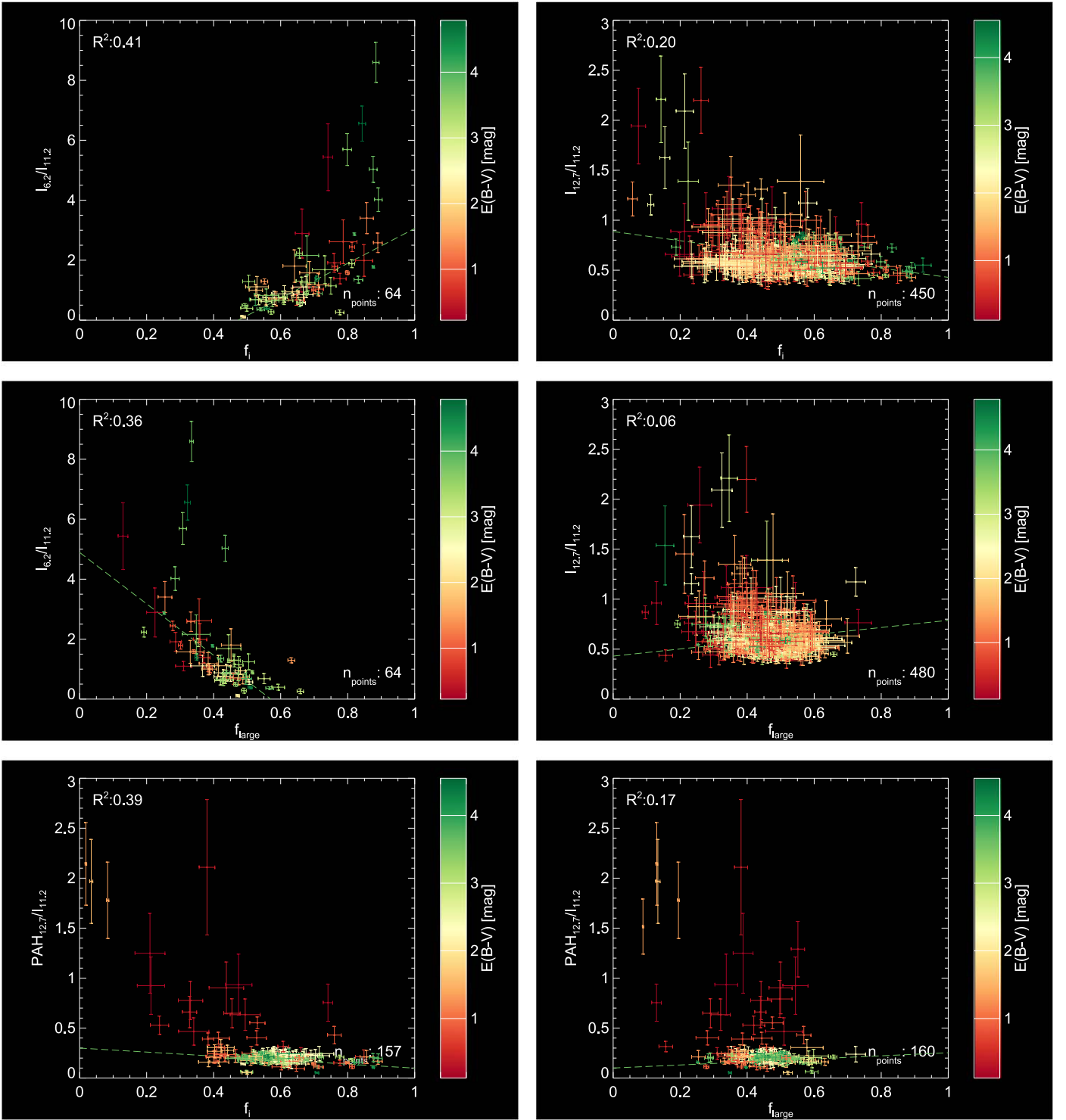


**Figure 14.** Top: the 6.2/11.2 (left) and 12.7/11.2  $\mu\text{m}$  (right) PAH band strength ratio vs. the PAHdb-derived ionization fraction ( $f_i$ ). Middle: the 6.2/11.2 (left) and 12.7/11.2  $\mu\text{m}$  (right) PAH band strength ratio vs. the PAHdb-derived large PAH fraction ( $f_{\text{large}}$ ). Bottom: the PAH<sub>12.7</sub>/ $I_{11.2}$   $\mu\text{m}$  PAH band strength ratio vs.  $f_i$  (left) and  $f_{\text{large}}$  (right). The data have a SNR  $\geq 3$  and  $0.06 \leq E(B - V) \leq 5.0$ . Trend lines determined by fitting the data have been overlain. For each correlation the linear correlation coefficient  $R^2$ , that takes uncertainties into account, has been provided. NB Some extraneous data have been clipped for presentation purposes. See Section 4.3 for details.

In general, but not across the board, the table shows the highest values of  $\gamma$  for the warmest dust temperatures. The lower values of  $\gamma$  are consistent with the warm neutral medium ( $\gamma \simeq 10^4 \text{ K}^{1/2} \text{ cm}^3$ ), with the others pushing into the photo-dissociation-region (PDR) domain ( $\gamma \simeq \text{few} \times 10^4 - 10^5 \text{ K}^{1/2} \text{ cm}^3$ ; A. G. G. M. Tielens 2005).

This shows that many of the background positions are not entirely isolated and are, to one degree or other, influenced by an additional radiation source rather than the interstellar radiation field alone. Obviously, the PDR-like backgrounds are far from isolated. By happenstance the off-target background position could have fallen on a nearby radiation source

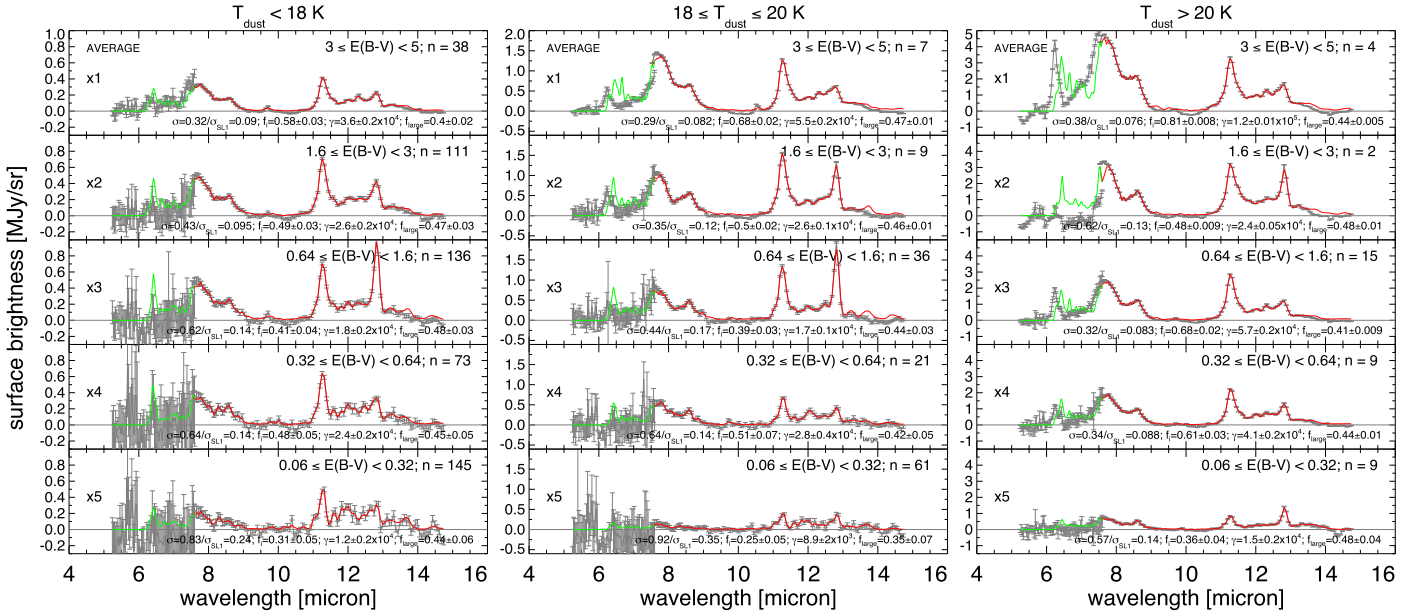


**Figure 15.** Average background PAH spectra across five  $E(B-V)$  and three  $T_{\text{dust}}$  bins. Only those background spectra with an uncertainty of less than  $3 \times 10^{-21} \text{ W cm}^{-2}$  for their  $11.2 \mu\text{m}$  PAH band strength and  $0.06 \leq E(B-V) \leq 5$  have been considered. The number of spectra in each bin is indicated by  $n$ . The average spectra (SL1+SL2 in gray) have been fitted (red = SL1, green = SL2) with PAH emission spectra synthesized using PAHdb. Indicated are the error ( $\sigma$  and  $\sigma_{\text{SL1}}$ ), ionization ( $f$ ) and large PAH fraction ( $f_{\text{large}}$ ), and the PAH ionization parameter  $\gamma$  determined from the fits through a Monte Carlo technique with the derived uncertainty given in parenthesis. See Section 4.4 for details.

**Table 1**

PAHdb-derived PAH Ionization Parameter  $\gamma$  for Different  $E(B-V)$  and  $T_{\text{dust}}$  Bins

$E(B-V)$	$\gamma [\times 10^4 \text{ K}^{1/2} \text{ cm}^3]$		
	$T_{\text{dust}} < 18 \text{ K}$	$18 \leq T_{\text{dust}} \leq 20 \text{ K}$	$T_{\text{dust}} > 20 \text{ K}$
0.06–0.32	$1.2 \pm 0.2$	$0.89 \pm 0.2$	$1.5 \pm 0.2$
0.32–0.64	$2.4 \pm 0.2$	$2.8 \pm 0.4$	$4.1 \pm 0.2$
0.64–1.6	$1.8 \pm 0.2$	$1.7 \pm 0.1$	$5.7 \pm 0.2$
1.6–3.0	$2.6 \pm 0.2$	$2.6 \pm 0.1$	$2.4 \pm 0.05$
3.0–5.0	$3.6 \pm 0.2$	$5.5 \pm 0.2$	$12 \pm 0.1$

or it was simply not sufficiently separated from the extended on-source target. This could indeed be easily the case for a close-by star-forming region like the Orion Molecular Cloud.

## 5. Astronomical Implications

A sizable fraction (18%;  $\text{SNR}_{11.2} > 3$ ) of the background spectra show detectable PAH emission, with the bulk (85%) in directions where  $0.06 \leq E(B-V) \leq 5.0$ .

While the correlation between PAHs and classical dust shown in Figure 7 appears at first glance to be poor, with a wide range in PAH emission strengths at all values of  $E(B-V)$ , the correlations of the  $11.2$  and  $12.7 \mu\text{m}$  PAH bands with WISE 12 Band 3 observations point to a much stronger connection. Figure 8 shows these bands plotted linearly against  $E(B-V)$ . As discussed in Section 4.1, these plots show temperature stratification and a linear upper bound relationship between the PAHs and classical dust.

All of the points along the upper boundary have high dust temperatures while points with lower temperature dust fills in below the upper bound. This implies that PAH abundances and dust densities are well correlated and that more intense radiation fields produce more PAH emission and warmer dust. This suggests that the PAH ionization parameter  $\gamma$ , which is

connected to the intensity of the radiation field through  $G_0$ , would correlate with dust temperature when assuming the electron density  $n_e$  and gas temperature  $T_{\text{gas}}$  are largely invariant. Though, while Table 1 indeed has the largest  $\gamma$ 's associated with the highest  $T_{\text{dust}}$  bins, a clear one-to-one correlation is lacking. Inspection of Figure 15 shows signs of Ne II  $12.8 \mu\text{m}$  emission in some of the averaged spectra (see also Section 4.2). This indicates possible contributions from ionized regions along those lines of sight and hence those values of  $\gamma$  may not be indicative of the isolated background ISM.

Each line of sight is a composite of all the material along each direction and consists of regions with differing densities and illumination. Those lines of sight with the lowest  $E(B-V)$  values can only be composed of low extinction regions, while those with high  $E(B-V)$  values could include a multitude of low, moderate, and high extinction regions. The lowest extinction lines of sight have low  $\gamma$ 's, indicative of the warm neutral phase of the ISM, while the other lines of sight are consistent with PAH emission from PDRs. In this case a PDR includes any cloud or filament surface with somewhat higher density than the warm neutral phase that is excited by nonionizing UV photons. Those directions that show obvious Ne II line emission must have a component that is illuminated by ionizing UV photons from luminous O and B stars.

One last thing to consider is the separation of the background from the intended science target and, on a larger scale, that from associated cloud structures. The former seems to be sufficiently scrutinized by the cross-dispersion profiles of the  $11.2 \mu\text{m}$  PAH emission, which are spatially completely unresolved for *all* backgrounds (Figure 4).

Concerning the latter, the presence of Ne II line emission in at least some of the background spectra does seem to indicate, not unexpectedly, that some of the backgrounds are associated with luminous O-B stars likely connected to larger extended structures. Appendix B examines this in more detail for the

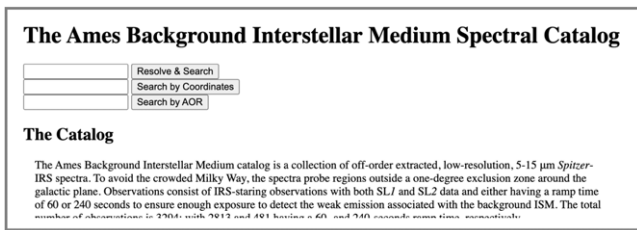


Figure 16. The Ames Background Interstellar Medium Spectral Catalog’s landing page showing the search interface.

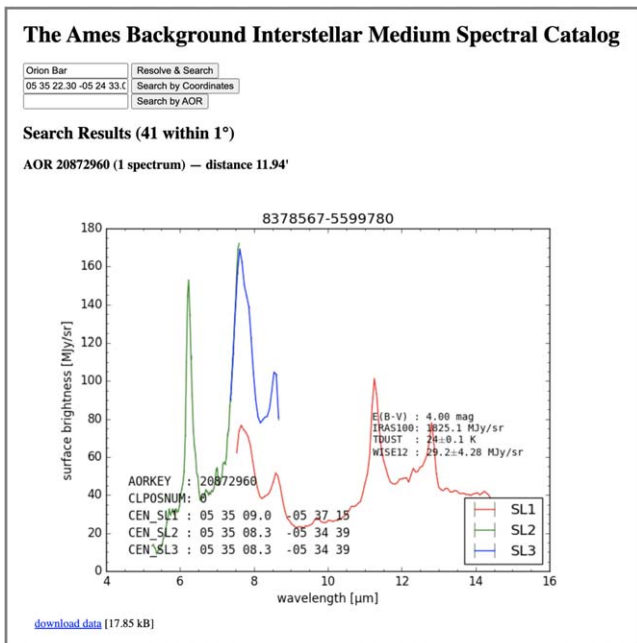


Figure 17. The Ames Background Interstellar Medium Spectral Catalog’s results page showing one of the non-dark-subtracted spectra found when searching for “Orion Bar.”

more diffuse backgrounds ( $0.06 \leq E(B - V) \leq 5.0$ ) by first spatially clustering by position and then constructing images of the 128 cluster regions from GAIA and WISE 12 full-sky dust maps. Indeed, many regions show the background positions to be associated with filamentary cloud-like structures.

## 6. The Ames Background Interstellar Medium Spectral Catalog

The Ames Background Interstellar Medium Spectral Catalog makes available the non-dark off-module extracted background spectra as well as a separate downloadable complementary table containing all derived measurement from this work.<sup>12</sup> Spectra can be retrieved using a known AOR key, by specifying coordinates, or by providing a target name that will be resolved using SIMBAD services. In the latter two cases the catalog is scanned at  $1^\circ$  increments from the resolved position until there is at least a single hit. Figure 16 shows the search interface as presented at the website.

Query results are organized per AOR key and the number of available spectra are indicated. For each result a spectrum is shown, with the orders color coded separately and associated

<sup>12</sup> The catalog can be accessed at <http://www.astrochemistry.org/bism>.

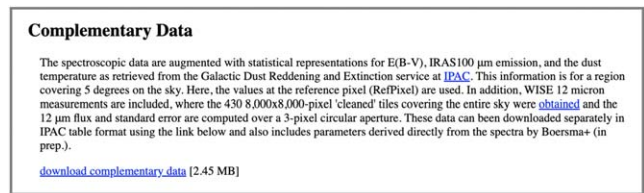


Figure 18. Ames Background Interstellar Medium Spectral Catalog website showing the link to the complementary data.

error bars. Also provided are the statistical representations for  $E(B - V)$ , IRAS100  $\mu\text{m}$  emission, the dust temperature as retrieved from the Galactic Dust Reddening and Extinction service at IPAC, and WISE12 measurements determined as described in this work. The spectra can be downloaded in IPAC format by clicking the “download data” link. The file size is indicated for convenience. Figure 17 shows an example when querying and resolving for “Orion Bar.”

The link to download the complementary data can be found near the bottom of the page, as is shown in Figure 18.

The website is written in PHP8 with SQLite3 as the database back-end and runs on Apache2 under Ubuntu Server 22.04 LTS. The figures and downloadable data have all been reproduced.

## 7. Summary and Conclusions

Many data sets obtained by the Spitzer-IRS contain “hidden” observations of the IR background ISM. These are often used to subtract line-of-sight contamination, or are simply ignored. Here, these background observations are considered in their own right. A catalog of 4090 spectra is constructed to examine the PAH spectral signature in the background ISM and its connection to extinction by (classical) dust.

To isolate any background PAH emission, carefully selected high-galactic latitude spectra, dominated by zodiacal light, were averaged and subtracted from the background data. Subsequently, the 6.2, 11.2, and 12.7  $\mu\text{m}$  PAH band strengths were determined. A strong, positive correlation is recovered between the 11.2  $\mu\text{m}$  PAH band strength with extinction ( $E(B - V)$ ) and WISE12 observations.

Focusing on the more diffuse emission with  $0.06 \leq E(B - V) \leq 5.0$ , correlations of the 6.2, 11.2, and 12.7  $\mu\text{m}$  PAH band strength is positive with  $E(B - V)$ , albeit with considerable scatter. In addition, the correlations reveal a clear separation into three distinct dust temperature regimes when presented on a linear scale. The correlations with WISE12 data are far better constrained.

Decomposition of the PAH emission in terms of charge and size using the data and tools made available through PAHdb reveals a tentative positive correlation between the 6.2/11.2  $\mu\text{m}$  PAH band strength ratio and  $f_i$ , while that with the 12.7/11.2  $\mu\text{m}$  PAH band strength ratio, surprisingly, hints to a slight negative trend. The 12.7/11.2  $\mu\text{m}$  PAH band strength ratio normally tracks with PAH ionization along with the 6.2/11.2  $\mu\text{m}$  PAH band strength ratio. Since the 11.2 and 12.7  $\mu\text{m}$  bands are also tracers for PAH edge structure and size, this behavior suggests PAH structures are changing along these lines of sight.

The relation between  $f_{\text{large}}$  and the 6.2/11.2  $\mu\text{m}$  PAH band strength ratio is negative, with that with the 12.7/11.2  $\mu\text{m}$  PAH band strength ratio hinting at being positive.

Increasing the SNR by averaging the background spectra into five  $E(B - V)$  and three  $T_{\text{dust}}$  bins shows a clear evolution

in the strength of the PAH emission and variations in the relative strength of the 11.2 and 12.7  $\mu\text{m}$  PAH bands. Database fits show, overall, an increase in  $f_i$  and  $\gamma$  but a somewhat more stable  $f_{\text{large}}$ . While the largest found  $\gamma$ s are associated with the highest  $T_{\text{dust}}$  bins, a clear one-to-one correlation is lacking. However, much of the analysis remains, in many cases, limited by the low SNR at shorter wavelengths ( $\lambda \lesssim 7.5 \mu\text{m}$ ).

Taking everything together, there are some hints that the PAH population in the more diffuse background behaves differently from that of the general ISM. However, in most cases the backgrounds are still associated with larger scale filamentary cloud-like structures or, in a few cases, PDR-like environments located somewhere along the line of sight.

The spectra and auxiliary data have been made publicly available for download through the Ames Background Interstellar Medium Spectral Catalog and, as they may guide JWST programs, focused on explicitly studying the (more diffuse) background ISM.

### Acknowledgments

C.B. is grateful for an appointment at NASA Ames Research Center through the San José State University Research Foundation (80NSSC22M0107). C.B., J.D.B., L.J.A., P.T. and A.M. acknowledge support from the Internal Scientist Funding Model (ISFM) Laboratory Astrophysics Directed

Work Package at NASA Ames (22-A22ISFM-0009). L.J.A., J.D.B., and A.M. are thankful for an appointment at NASA Ames Research Center through the Bay Area Environmental Research Institute (80NSSC19M0193).

*Facility:* Spitzer.

*Software:* astropy (Astropy Collaboration et al. 2013, 2018), amesphdbidsuite (C. W. Bauschlicher et al. 2018).

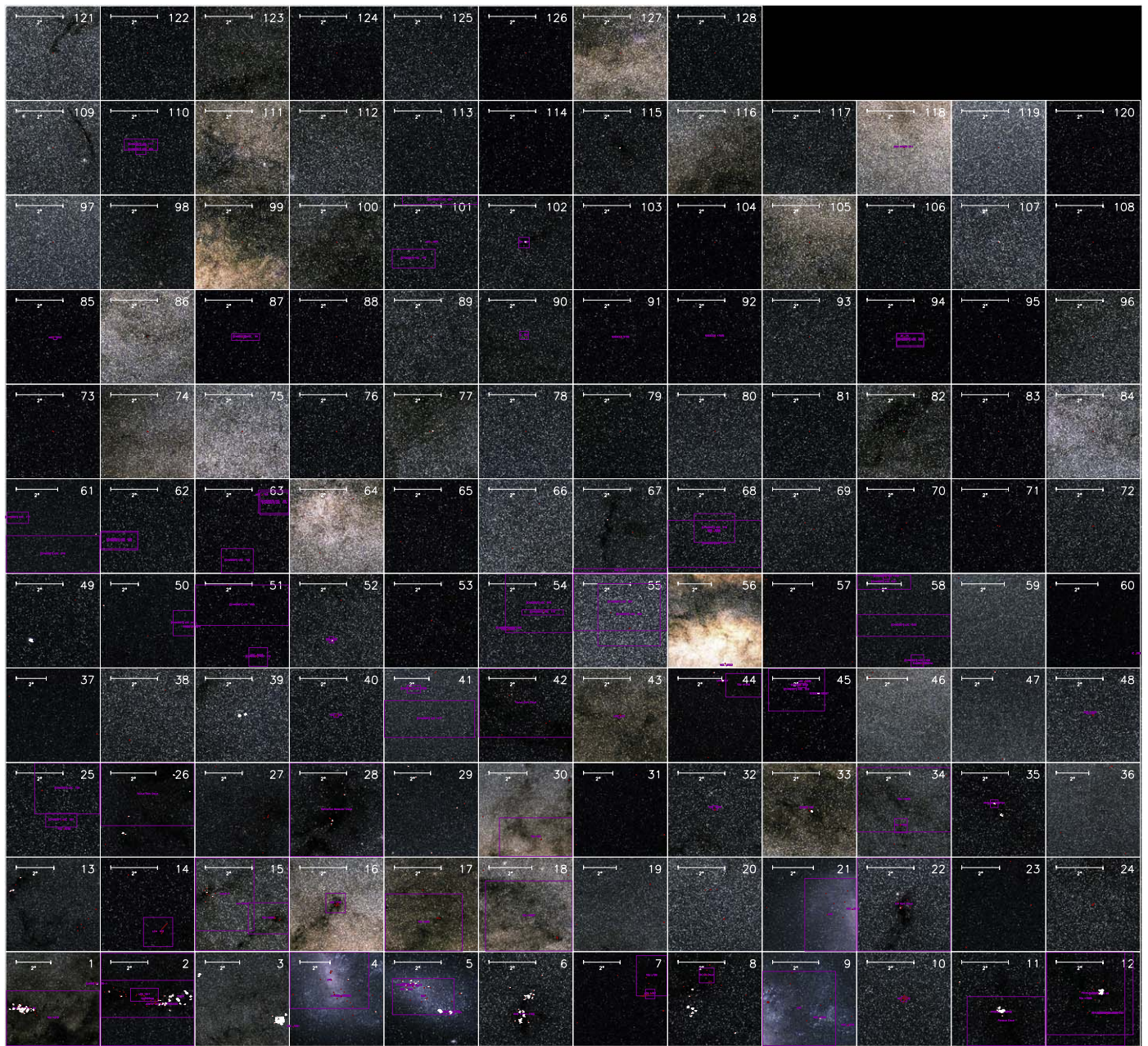
## Appendix A Observations with Complications

Table A1 lists and provides a brief description of those observations for which analysis complications were encountered.

**Table A1**  
Observations with Complications

AOR Key	Description
14136064	no BCD files
23039488	no BCD files
26086912	CUBISM “no fluxcon ...” error (for NODARK)
23796224	CUBISM “no fluxcon ...” error (for NODARK)
23795968	NULL-pointer reference in CUBEPROJ::BUILDCUBE 4265 (for NODARK)





**Figure 20.** Zoom-in on the 128 cluster regions from Figure 20 using the  $40k \times 20k$  GAIA all-sky image. Scale bars indicate  $2^\circ$ . The background positions are shown as the red points, in white nearby SIMBAD IR sources, and in blue those with known sizes. Parent objects are indicated in purple, clipped to the extent of the field of view. Acknowledgment: Gaia Data Processing and Analysis Consortium (DPAC); A. Moitinho / A. F. Silva / M. Barros / C. Barata, University of Lisbon, Portugal; H. Saviotto, Fork Research, Portugal.

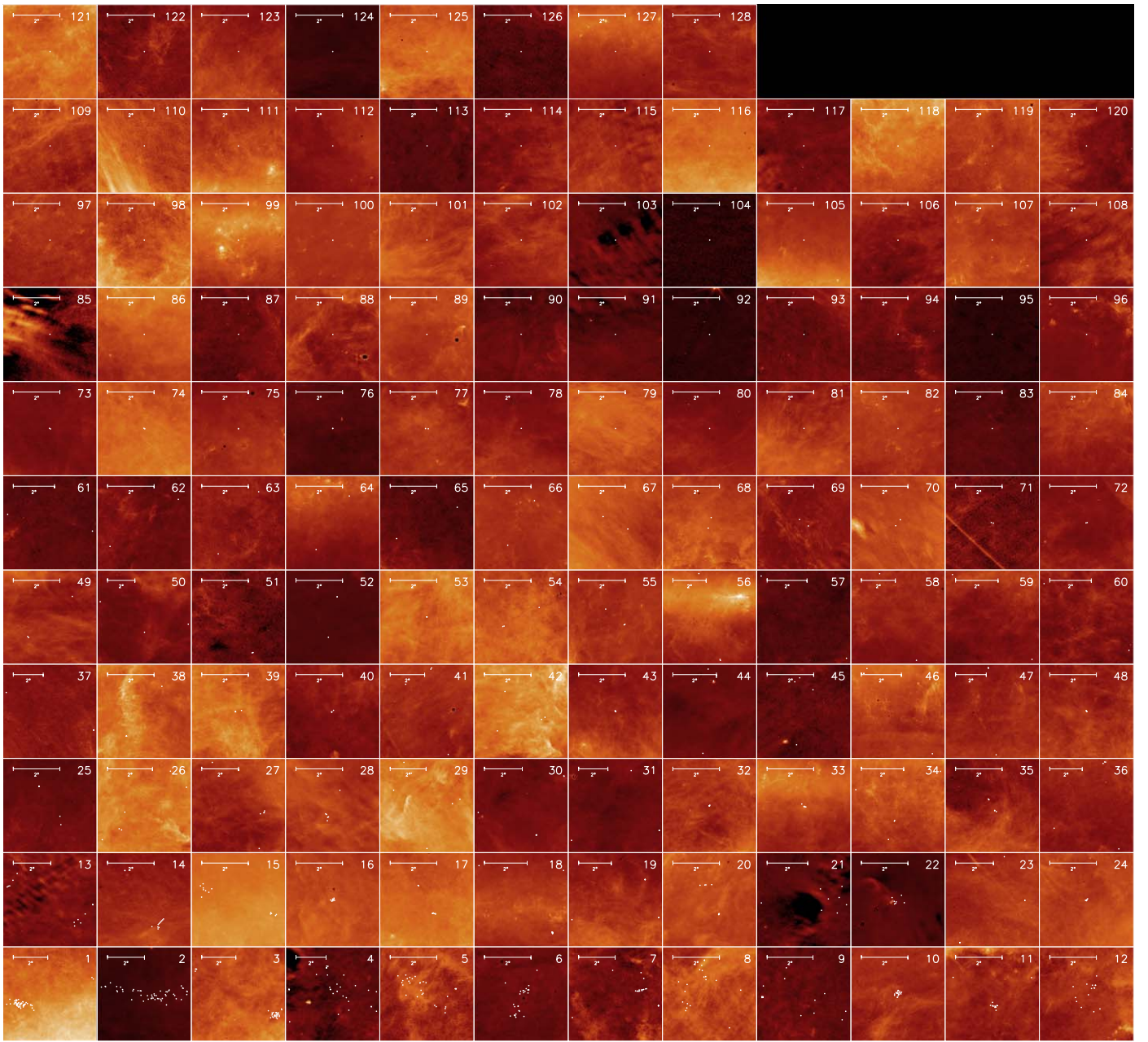


**Figure 21.** Zoom-in on the 128 cluster regions from Figure 19 using the  $430, 8000 \times 8000$  pixel “cleaned” tiles from the WISE  $12 \mu\text{m}$  full-sky dust map. Scale bars indicate  $2^\circ$ . The background positions are shown as the white points. Each image is displayed using a logarithmic scaling.

**ORCID iDs**

C. Boersma  <https://orcid.org/0000-0002-4836-217X>  
 J. D. Bregman  <https://orcid.org/0000-0002-1440-5362>  
 L. J. Allamandola  <https://orcid.org/0000-0002-6049-4079>  
 P. Temi  <https://orcid.org/0000-0002-8341-342X>  
 A. Maragkoudakis  <https://orcid.org/0000-0003-2552-3871>

**References**

- Astropy Collaboration, Price-Whelan, A. M., Sipőcz, B. M., et al. 2018, *AJ*, **156**, 123
- Astropy Collaboration, Robitaille, T. P., Tollerud, E. J., et al. 2013, *A&A*, **558**, A33
- Bauschlicher, C. W., Boersma, C., Ricca, A., et al. 2010, *ApJS*, **189**, 341
- Bauschlicher, C. W., Ricca, A., Boersma, C., & Allamandola, L. J. 2018, *ApJS*, **234**, 32
- Boersma, C., Bauschlicher, C. W., Ricca, A., et al. 2014a, *ApJS*, **211**, 8
- Boersma, C., Bregman, J., & Allamandola, L. J. 2014b, *ApJ*, **795**, 110
- Boersma, C., Bregman, J., & Allamandola, L. J. 2015, *ApJ*, **806**, 121
- Boersma, C., Bregman, J., & Allamandola, L. J. 2016, *ApJ*, **832**, 51
- Boersma, C., Bregman, J., & Allamandola, L. J. 2018, *ApJ*, **858**, 67
- Bregman, J., & Temi, P. 2005, *ApJ*, **621**, 831
- Hony, S., Van Kerckhoven, C., Peeters, E., et al. 2001, *A&A*, **370**, 1030
- Houck, J. R., Roellig, T. L., van Cleve, J., et al. 2004, *ApJS*, **154**, 18
- IRSA 2022, Galactic Dust Reddening and Extinction, NASA IPAC DataSet, IRSA537, doi:10.26131/IRSA537
- Lan, T.-W., Ménard, B., & Zhu, G. 2015, *MNRAS*, **452**, 3629
- Maragkoudakis, A., Boersma, C., Temi, P., Bregman, J. D., & Allamandola, L. J. 2022, *ApJ*, **931**, 38
- Mattioda, A. L., Hudgins, D. M., Boersma, C., et al. 2020, *ApJS*, **251**, 22
- Meisner, A. M., & Finkbeiner, D. P. 2014, *ApJ*, **781**, 5
- Onaka, T., Yamamura, I., Tanabe, T., Roellig, T. L., & Yuen, L. 1996, *PASJ*, **48**, L59
- Shannon, M. J., Stock, D. J., & Peeters, E. 2015, *ApJ*, **811**, 153
- Smith, J. D. T., Armus, L., Dale, D. A., et al. 2007, *PASP*, **119**, 1133
- Tanaka, M., Matsumoto, T., Murakami, H., et al. 1996, *PASJ*, **48**, L53
- Tielens, A. G. G. M. 2005, *The Physics and Chemistry of the Interstellar Medium* (Cambridge: Cambridge Univ. Press) doi:10.1017/cbo9780511819056
- Werner, M. W., Roellig, T. L., Low, F. J., et al. 2004, *ApJS*, **154**, 1